Journal of Biomedical Optics

SPIEDigitalLibrary.org/jbo

Confocal microscopy with strip mosaicing for rapid imaging over large areas of excised tissue

Sanjee Abeytunge
Yongbiao Li
Bjorg Larson
Gary Peterson
Emily Seltzer
Ricardo Toledo-Crow
Milind Rajadhyaksha

SPIE

Confocal microscopy with strip mosaicing for rapid imaging over large areas of excised tissue

Sanjee Abeytunge,[a] Yongbiao Li,[a] Bjorg Larson,[b] Gary Peterson,[b] Emily Seltzer,[c*] Ricardo Toledo-Crow,[a*] and Milind Rajadhyaksha[b*]
[a]Memorial Sloan-Kettering Cancer Center, Research Engineering Laboratory, New York, New York 10065
[b]Memorial Sloan-Kettering Cancer Center, Dermatology Service, New York, New York 10022
[c]Livingston High School, Livingston, New Jersey 07039

Abstract. Confocal mosaicing microscopy is a developing technology platform for imaging tumor margins directly in freshly excised tissue, without the processing required for conventional pathology. Previously, mosaicing on 12- × -12 mm^2 of excised skin tissue from Mohs surgery and detection of basal cell carcinoma margins was demonstrated in 9 min. Last year, we reported the feasibility of a faster approach called "strip mosaicing," which was demonstrated on a 10- × -10 mm^2 of tissue in 3 min. Here we describe further advances in instrumentation, software, and speed. A mechanism was also developed to flatten tissue in order to enable consistent and repeatable acquisition of images over large areas. We demonstrate mosaicing on 10- × -10 mm^2 of skin tissue with 1-μm lateral resolution in 90 s. A 2.5- × -3.5 cm^2 piece of breast tissue was scanned with 0.8-μm lateral resolution in 13 min. Rapid mosaicing of confocal images on large areas of fresh tissue potentially offers a means to perform pathology at the bedside. Imaging of tumor margins with strip mosaicing confocal microscopy may serve as an adjunct to conventional (frozen or fixed) pathology for guiding surgery. [DOI: 10.1117/1.JBO.18.6.061227]

Keywords: confocal microscopy; mosaicing; strip mosaicing; tissue flattening; Mohs surgery; lumpectomy; mastectomy; surgical pathology.

Paper 12656SS received Oct. 1, 2012; revised manuscript received Dec. 19, 2012; accepted for publication Dec. 21, 2012; published online Feb. 6, 2013.

1 Introduction

The accurate and complete removal of tumor, with minimal removal of healthy surrounding tissue, is guided by the examination of pathology. The preparation of pathology, either during surgery or after, is time-consuming and labor-intensive. In the setting of nonmelanoma skin cancers, frozen pathology that is prepared during Mohs surgery requires 20 to 45 min per excision, and two or more excisions are performed, such that the total preparation time lasts from two to several hours.[1] In other settings such as with head-and-neck and breast cancer, fixed pathology is prepared after surgery. Preparation of fixed sections requires one to two days. Since it takes such a long time to obtain pathology results, the patient is sent home immediately after surgery. If the pathology shows positive tumor margins, the patient must undergo additional surgery (resection), and/or radiotherapy or chemotherapy. The incomplete removal of tumor and positive margins are reported to occur in 20 to 70% of patients, depending on the surgical setting.[2,3] Although the rates of resections can be reduced by aggressive removal of tissue from a wide margin around the tumor, it can affect the functionality of the organ or produce unacceptable aesthetical results for the patient. Therefore the objective is to minimize the removal of healthy tissue by reducing the margins and still perform complete removal of the tumor. To address this problem, high-resolution optical imaging methods capable of displaying nuclear and cellular morphology, offer the possibility for rapid detection of tumors in large areas of freshly excised or biopsied tissue. Currently, confocal microscopy, full-field optical coherence tomography, multispectral macro-imaging, multiphoton microscopy, fluorescence lifetime imaging and other approaches are being developed for this purpose.[4–16,17]

We have been developing confocal mosaicing microscopy as a technology platform for imaging tumor margins in fresh tissue excisions from surgery[2,3,13–15] to provide high-resolution images of large areas of tissue within minutes. Previously, we collected square-shaped images with aspect ratios of ~1 : 1, and stitched them together with custom software into a mosaic to display a large field of view. Mosaicing of 36- × -36 images to display 12- × -12 mm^2 of excised tissue from Mohs surgery was demonstrated in 9 min.[13–15] In a blinded examination of 45 fluorescence mosaics by two Mohs surgeons, basal cell carcinoma margins were detected with an overall sensitivity of 96.6% and a specificity of 89.2%.[18,19] The results of this preclinical study demonstrated the promise of confocal mosaicing microscopy.

Although 9 min is certainly faster than the hours or days required for preparing conventional (frozen or fixed) pathology, routine implementation in surgical settings will require shorter processing times. The unequivocal feedback from surgeons was that this technology was unlikely to be adopted unless the speed was improved. The clear expectation was that to reach practical and routine use in any operating room setting, mosaicing must meet the surgeons' need to examine tumor margins in large areas (~cm^2) within a few minutes. To address this need we designed a faster approach called "strip mosaicing." The initial instrumentation work for strip mosaicing was reported last year.[20] Strip

*Equal contribution (shared senior authorship).

Address all correspondence to: Sanjee Abeytunge, Memorial Sloan-Kettering Cancer Center, Research Engineering Laboratory, New York, New York 10065. Tel.: 212-6393212; Fax: (212) 717-3604; E-mail: abeytuns@mskcc.org

mosaicing is performed with a combination of optical and mechanical scanning. The tissue is mechanically translated across a linearly scanned focused laser beam. This approach is faster because the speed of mosaicing strips is primarily governed by the fast line acquisition rate in the confocal microscope[20] and does not use the single frame acquisition method previously reported.[14,18]

In this paper, we report further advances and enhancement of the electronics and mechanics, the development of custom software, and the overall integration of hardware and software into an approach that demonstrates imaging of 1- × -1 cm^2 of human skin tissue with 1-μm lateral resolution in 90 s and 5.5- × -3.5 cm^2 of breast tissue with 0.8-μm lateral resolution in 13 min. The enhancements include a device to mount and flatten fresh tissue from surgery, improvements in the tissue translation stage for speed, accuracy and precision, synchronization of the optical and mechanical scanning to optimize alignment among and registration of strips, and stitching of image strips in parallel with acquisition using custom software.

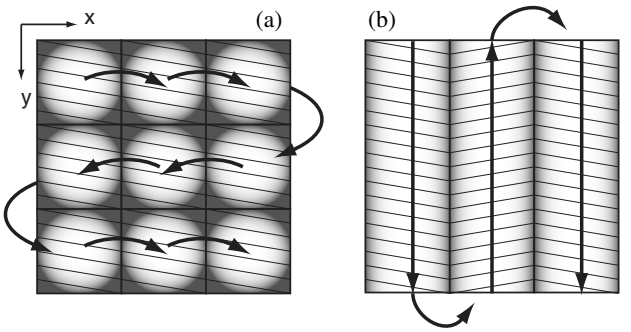

Fig. 1 Comparison of mosaicing concepts: (a) mosaicing of square-shaped images in two dimensions; (b) mosaicing of rectangular-shaped long strips in one dimension (this figure is reproduced from Ref. 20).

2 Materials and Methods

2.1 *Mosaicing Method*

Our previous mosaicing method required stitching square-shaped images, with ~1:1 aspect ratio, in two dimensions, as shown in Fig. 1(a). The newly developed method acquires rectangular-shaped long strips of images,[20] with 1:25 aspect ratio for a 10-mm long strip, and stitches along the length of the strip as shown in Fig. 1(b). The elimination of a stitching dimension reduces the processing time and the artifacts due to illumination fall-off by half.

The strip mosaicing scheme, with combined optical and mechanical scanning, is shown in Fig. 2. The fast optical scanner produces a scan-line (in the x direction) that defines the width of a strip. Scanning the length of the strip (in the y direction) is performed by translating the stage in the direction orthogonal to the line. When the acquisition of a strip image is completed ("forward scan" in y direction), the stage moves in the x direction a distance equal to or less than the width of the strip. Then the stage moves along the strip length but in the opposite direction ("return scan"), and another strip image is acquired. This process of acquiring strip images, sequentially in opposite y directions (forward scan followed by return scan) is repeated until the entire tissue is imaged. The aspect ratio of a strip is restricted only by the mechanical limits of the scanning stage.

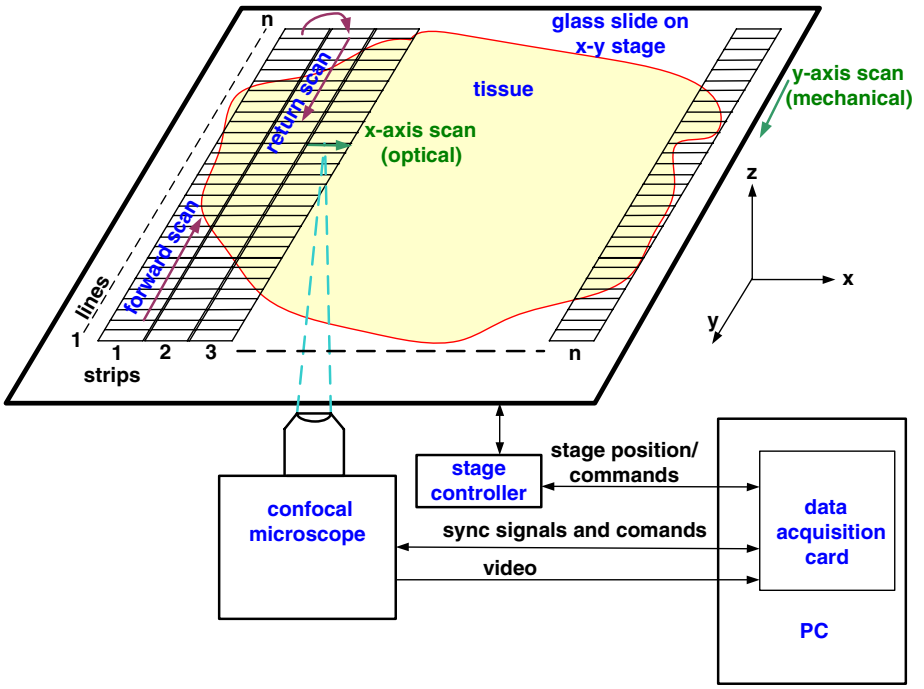

Fig. 2 Schematic of the strip-scanning mechanism. The fast optical scan (x axis scan) defines the width of a strip. The slow mechanical scan along the length of the strip (y axis scan) is performed by translating the stage in the direction orthogonal to the x axis. When the acquisition of a strip image is completed ("forward scan"), the stage moves in the x direction a distance equal to or less than the width of the strip. Then the stage moves along the strip length, but in the opposite direction ("return scan"), and another strip image is acquired. This process of acquiring strip images is repeated until the entire tissue is imaged.

2.2 *Instrumentation*

2.2.1 *Confocal microscope*

Our system is based on a modified breadboard version of a commercial confocal microscope (Vivascope 2000, Lucid Inc, Rochester, NY). Details are available in our earlier papers.[13–15,18,19] The microscope is set up to acquire images in fluorescence. The microscope is in an inverted configuration designed to image excised or biopsied tissue *ex vivo*. The illumination is from a 488-nm laser that delivers ~5 mW on the tissue. A 24-sided polygonal mirror scans the laser in the x direction sweeping a line at ~8.9 kHz through a 30×, 0.75 numerical aperture (NA) water immersion objective lens (StableView, Lucid Inc.) The length of the scanned line, which defines the width of the strip, is 485 μm. The theoretical lateral resolution, according to the Rayleigh criterion, is 0.4 μm (Airy radius) and the expected diffraction-limited optical sectioning is 2.3 μm. The objective lens is custom-designed to image through a 1-mm-thick glass slide. In normal operation, this line is optically scanned in the orthogonal direction (y direction) by a galvanometrically driven mirror to produce a square image. To acquire a long rectangular-shaped strip image, we center and lock the position of the stop the galvanometric scanner.

2.2.2 *Mechanical stage*

The mechanical specifications of the translation stage, such as straightness, flatness, repeatability and accuracy are important factors for long strip scans. We use a high-quality dual-axis stage (BioPrecision2, Ludl Electronics Products, Hawthorne, NY) to mechanically translate the tissue with respect to the objective lens. The straightness and flatness of this stage is 1 μm/25 mm. Therefore, for a translation of 10-mm travel, the maximum deviation in straightness is 0.8 μm between any two strips. This is well within the overlap between any two strips. The maximum deviation in flatness is also within the optical sectioning of 2.3 μm.

The translation stage is equipped with a position encoder (MAC5000, Ludl). The encoder outputs are sent to a fast data acquisition card for synchronization in real time. The commands to initiate and control the movement of stages are sent to the controller through a USB bus.

2.2.3 *Synchronization of strips in the y direction*

In our earlier configuration,[20] the translation stage mechanical scan (slow scan in y direction) was driven by a stepper-motor without a position encoder. We accomplished the synchronization of the polygon driven optical scan (fast scan in x direction) and the translation stage mechanical scan (slow scan in y direction) by counting the steps from the stepper-motor. This method turned out to be unreliable. We observed mismatch of up to 75 lines, between any two strips, due to missing steps in the motors and the resulting lack of position accuracy. This mismatch was corrected with software during stitching of the strips but at the expense of more computer processing and increased time for creating mosaics. However, the current position synchronization in the y direction reduces the work of the stitching algorithm, thus reducing the time required to complete the mosaic. The synchronization mechanism that we report in this paper ensures that the theoretical maximum mismatch between any two strips is one line in the y direction. Figure 3 shows the synchronizing scheme for the strips.

2.2.4 *Tissue flattening and stage leveling*

In order to image a large area, the surface of the tissue is scanned in a two-dimensional (2-D) "image plane," which is perpendicular to the optical axis of the objective lens in the microscope (Fig. 4). However, surgically excised tissue has a

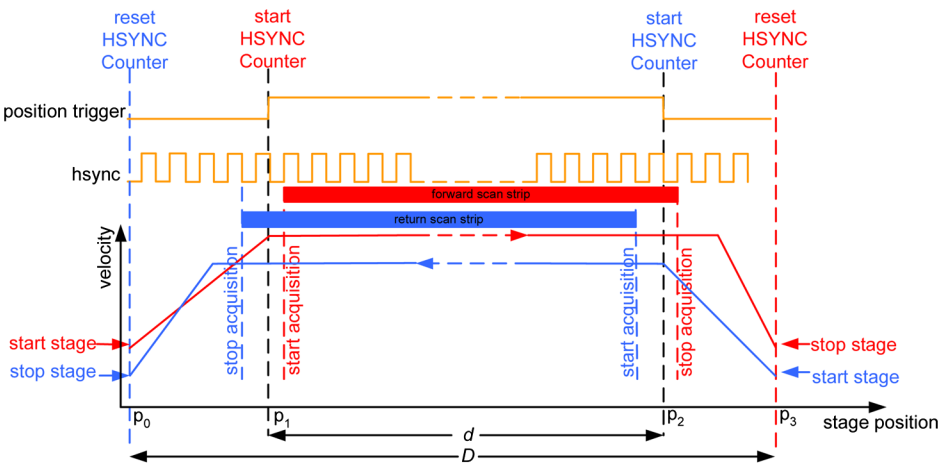

Fig. 3 The synchronizing scheme for the strips. A y translation stage cycle consists of two mechanical movements that produce two image strips: the "forward scan" P_0 to P_3, and the "return scan" P_3 to P_0. The velocity profiles are depicted in red for the forward movement, and blue for the return. The image is acquired within the constant velocity portion (d), between P_1 and P_2, of the scans. This avoids distortion of the mosaic due to compression or elongation of pixels. Therefore, we choose a scan distance (D) for the y translation stage such that the region of constant velocity (d) is larger than the size of the tissue sample. After the forward scan is initiated and the stage reaches P_1, the "position trigger" signal is asserted to arm the counter that monitors horizontal synchronization pulses (HSYNC) from the asynchronous optical scanner. When the HSYNC counter receives the next HSYNC pulse, the data acquisition begins. When the stage reaches P_2, the HSYNC counter resets and the acquisition continues until the last line is complete in the strip image. Then the stage decelerates and stops at P_3. Once the x translation stage moves in the x direction to a predetermined position that sets the width of the strip and the overlap between adjacent strips, the return scan is initiated from P_3 to P_0. It follows a similar mechanism to the forward scan. This cyclical process, forward scan and return scan, is repeated until the entire tissue is imaged.

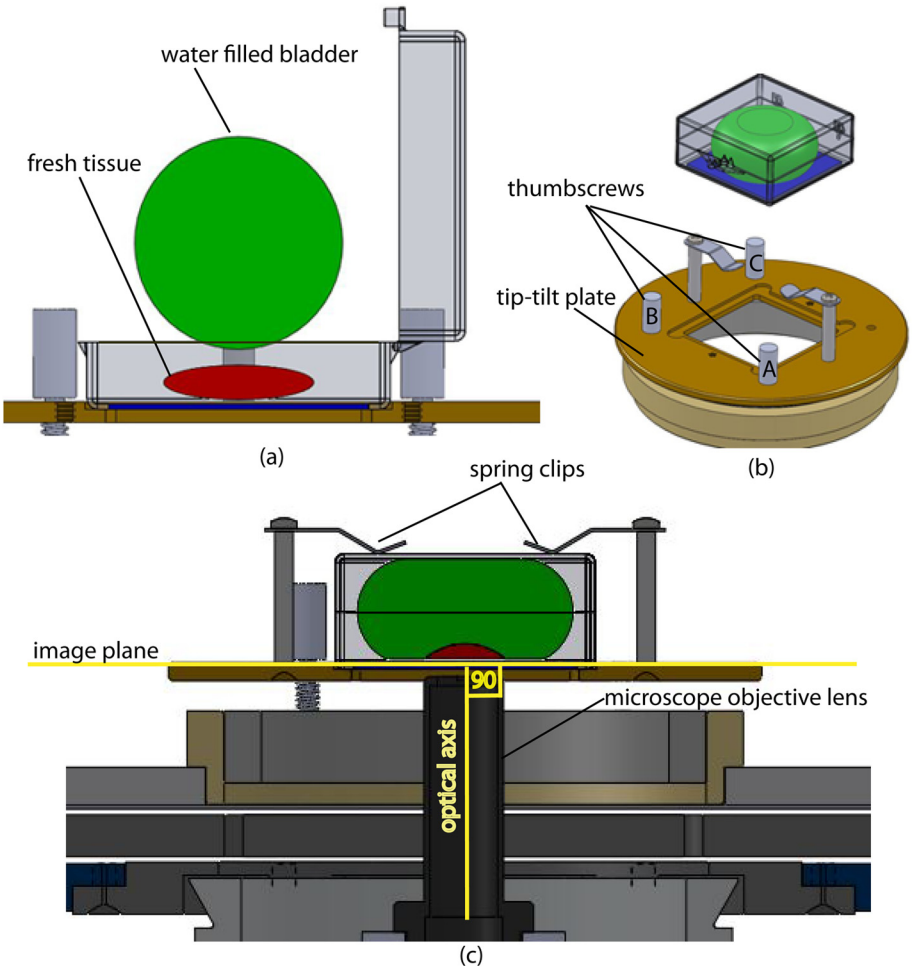

Fig. 4 Schematic representation of the tissue-flattening device: (a) 2-D view of the tissue (in red) inside the cassette in its natural shape, as often seen in Mohs surgical excisions, with the edges curved up from the image plane and the lower (to be imaged) surface not flattened. The cassette is shown to be open with no force is applied to the water-filled bladder; (b) view of the closed tissue-cassette before mounting on the tip-tilt plate; the thumbscrews A, B, and C can be used to adjust the tip and tilt of the image plane relative to the optical axis, so as to orient the two at exactly 90 deg to each other; (c) schematic representation shows how the tissue is flattened, relative to the image plane and optical axis, by the water filled bladder when force is applied to it.

three-dimensional (3-D) topography with varying shape and size. Furthermore, the tissue has variable mechanical compliance; for example, skin tissue is relatively stiff whereas breast tissue is soft and gel-like. This requires that the tissue surface be flattened onto a 2-D plane that conforms to the image plane of the microscope [Fig. 4(c)]. For this purpose we designed a tissue flattening and mounting device, as shown in Fig. 4(a).

We use a rubber bladder filled with water to flatten the tissue onto a 1-mm-thick BK7 window inside a cassette Fig. 4(a). To flatten the desired (lower) surface, the user places the tissue at the center of the cassette, the water-bladder on top and closes the cassette cover. Then the tissue-cassette is placed on the tip-tilt plate, secured with two spring-loaded clips and placed on the microscope.

Acquisition of a large number of images over a large area at constant depth requires the imaging and scanning planes to be coincident. This is obtained by adjusting the tip-tilt plate with spring-loaded thumbscrews [Fig. 4(b)]. The three thumbscrews are placed at right angles to each other, and tip/tilt can be adjusted by initially turning either thumbscrew A or C [Fig. 4(a)], while observing images of the glass window at four corners. The image of the window may be either a circular spot when focused on the surface or a ring due to field curvature when focused past the glass. This adjustment is performed in an iterative manner until the images at the four corners appear identical to each other. This device and the alignment method allow large tissues to be matched to the image plane of the microscope, and enables mosaicing over large areas. The mounting of the tissue cassette and the adjustment of the tip-tilt are robust enough to allow repeatable operation during extended periods without the need to realign.

2.2.5 *Tissue preparation*

Discarded excisions skin and breast tissues were obtained under two IRB-approved protocols. The Dermatology Service provided discarded tissue from Mohs surgery, and breast tissue was obtained from The Evelyn H. Lauder Breast Center at Memorial Sloan-Kettering Cancer Center (MSKCC). Details about collection and handling of the tissues from Mohs surgery and staining methods have been extensively described in our earlier papers.[14,21] The staining of nuclear morphology is accomplished by soaking the tissue in 0.6-mM acridine orange for 30 s for skin tissue and 1 min for breast tissue, followed by

rinsing the excess with isotonic phosphate buffered saline solution.

2.3 *Acquisition of Mosaics*

For acquisition of mosaics, the resolution is set in our acquisition system to the level of nuclear and other morphologic detail needed to match standard histology. While relatively lower resolution may be adequate for imaging skin tissue, higher resolution is needed to analyze breast tissue.

The images are acquired in LabView and displayed in 8-bits. The 8-bit pixel depth was chosen because of our previous experience and for practical reasons. Clinical results from our previous studies[18,19] have validated that 8-bits are sufficient for this particular application. Our Mohs surgeons found the quality of the resulting images to be clinically acceptable and were able to evaluate mosaics, in a manner similar to their reading of histopathology, with sensitivity of 96.6% and specificity of 89.2%. Another consideration is that 8-bit mosaics of large areas produce images of 300 to 400 MB. Increasing the depth to

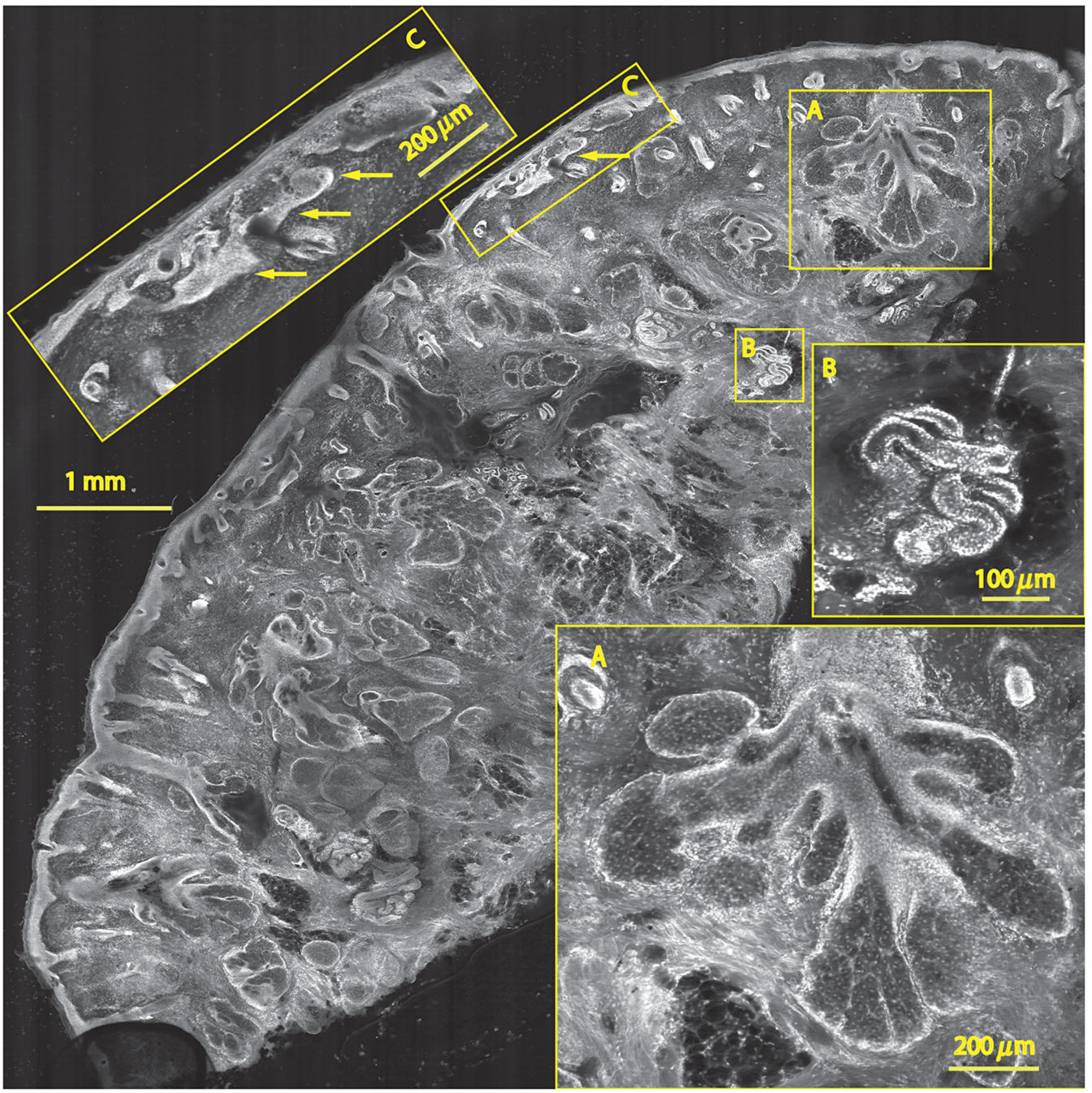

Fig. 5 A 7.7- × -7.7 mm^2 mosaic consisting of 24 fluorescence image strips of excised tissue from Mohs surgery. Typical features such as sebaceous glands (a) and eccrine glands (b) can be seen. Nests of superficial basal cell carcinomas (c) shown with arrows are observed, showing increased density of nuclei. The mosaic dimensions are 8100- × -8100 pixels (width x height) with 8 bits/pixel. Note that the magnified areas are display zooms obtained from the original image showing the detail and resolution of the mosaic. The features in the mosaic compare well, in general, to the pathology (Fig. 6) in terms of location, shape, size, nuclei of cells (shown in bright white) and overall morphology of both basal cell carcinomas and normal features.

16-bits would double their size making them difficult to manipulate. Such large image files pose practical challenges for subsequent processing and storing. This is further addressed in Sec. 2.5 on display of mosaics. The fluorescence images are captured with a fast DAQ card (PCI-6115 and Labview, National Instruments, Austin TX). The captured image strips are stitched with custom software developed by our group.

2.3.1 *Mosaics of skin tissue*

The acquisition time is limited by the speed of the optical (polygon) scanning rate of ~8.9 kHz. The line is sampled with a 6.5-MHz pixel clock. Our theoretical lateral resolution (Airy radius) is ~0.4 μm. For the resulting spot diameter of ~0.8 μm, adequate sampling requires two lines per resolvable distance, which requires the speed of the mechanical stage to be less than 1.8 mm/s [(0.4 μm/2)×8.9 kHz]. However, we scan our stage at ~8.5 mm/s and choose to under-sample by a factor of about 4.7 to reduce the acquisition time. This results in a pixel size of ~1 μm in both x and y directions. This is adequate for the interpretation of images of skin by Mohs surgeons and pathologists, as was explained in our earlier paper.[20] Once the y scan is completed, the x stage moves 400 μm laterally, leaving approximately a 19% overlap between any two strips. We repeat this process until the tissue is fully scanned.

2.3.2 *Mosaics of breast tissue*

The evaluation of breast tissue demands higher lateral resolution. To achieve a higher resolution, we slowed the polygon scan speed to 6.5 kHz, while holding sampling pixel clock at 6.5 MHz, thus slowing the acquisition time of a strip. To maintain adequate sampling, we must scan the mechanical stage at ~1.3 mm/s [(0.4 μm/2) × 6.5 kHz]. However, we move the stage at 5 mm/s, which results in under-sampling of about 3.8. At this stage speed, the resulting pixel size is ~0.8 μm in both x and y directions. The lateral move of the x stage is 480 μm.

2.4 *Stitching of Image Strips*

A stitching algorithm was written in Matlab (R2011a, Mathworks, Inc.) to automatically register image strips in the order in which they are collected. The stitching algorithm has three parts: a registration algorithm, an intensity fall-off correction, and blending in the overlap region between the two strips.

The strip-scanning method, as compared with the traditional mosaicing method, simplifies registration of images, as each image needs to be registered to only one neighbor instead of two. Strips are registered pair-wise using a phase correlation method chosen for speed and ease of implementation, as it is easily computed by fast Fourier transform (FFT). Computing the phase correlation between the two images produces a 2-D matrix of correlation values where the coordinate of each value in the correlation matrix corresponds to a possible offset between the two images. The correlation value is maximal at the coordinate at which the same features in the two images overlap. But, because the correlation of two rectangular functions (such as two images) is a triangle function, the correlation is biased toward solutions near zero offset between the two images (the peak of the triangle). The bias is removed in the x direction by dividing the phase correlation matrix by a triangle function. The removal of the bias emphasizes the noise near the edges of the correlation matrix, where solutions of maximal offset between the two images lie. Solutions of maximal offset correspond to no overlap between the images. Because we expect the images to overlap by an amount that is set by the stage motors, we can exclude solutions outside of the expected range. Therefore coordinates in the noisy region near the edges of

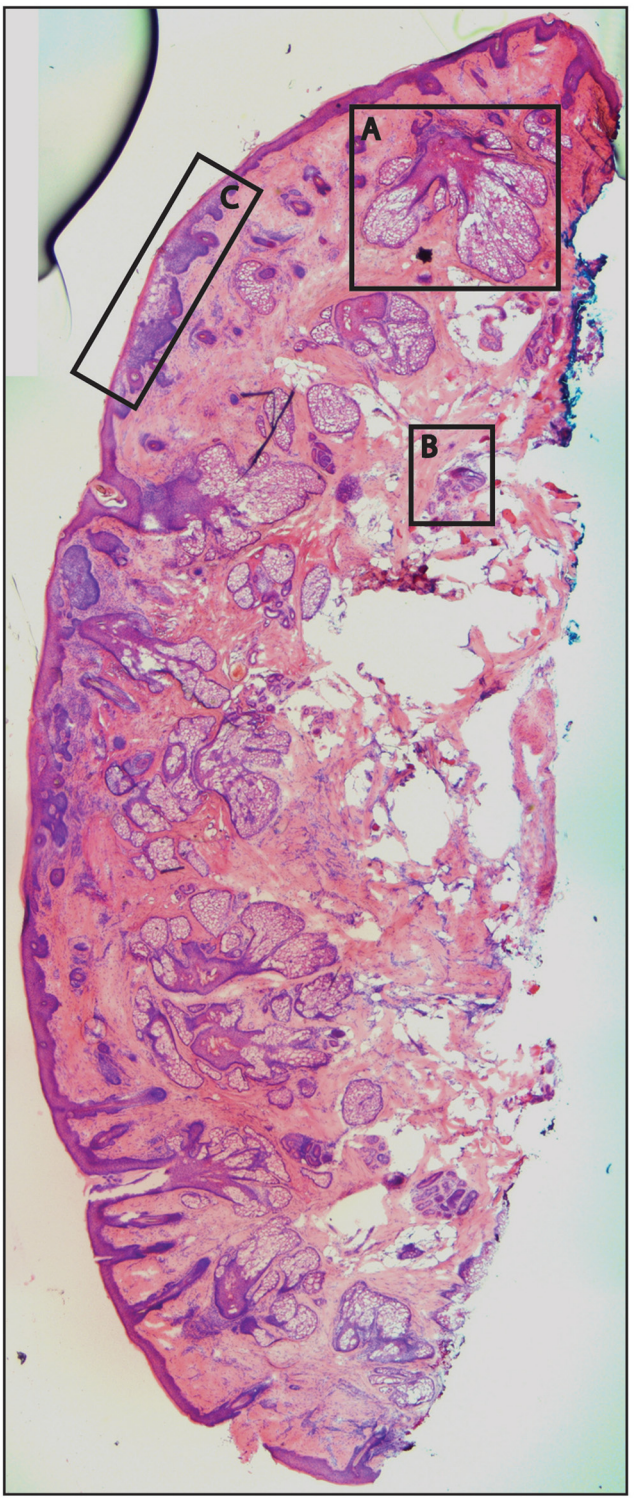

Fig. 6 Frozen H&E-stained pathology of excised tissue from Mohs surgery. This frozen section corresponds to a tissue slice that is adjacent to (but not exactly of) the imaged surface shown in Fig. 5. The features in inset areas A, B, and C are clearly identified across the two figures.

the correlation matrix are excluded from the search region. In the *y* direction, we expect solutions near zero offset, and therefore the removal of the bias was determined to be unnecessary along the *y* direction. The solution for *x* offset and *y* offset between the two images is found by determining the maximum of the correlation matrix after the bias has been removed and the edges of the matrix have been excluded from the search region.

Performing a 2-D FFT on very large images requires a large amount of memory. In practice, only a small section of the strip is required to perform registration, as long as the chosen *y* length of the section is greater than the *y* offset between the two strips. The chosen strip section must contain features to register. In our setup, the tissue lies in the center of the glass window. Hence, a section that is 10 to 30% the length of the strip is chosen from

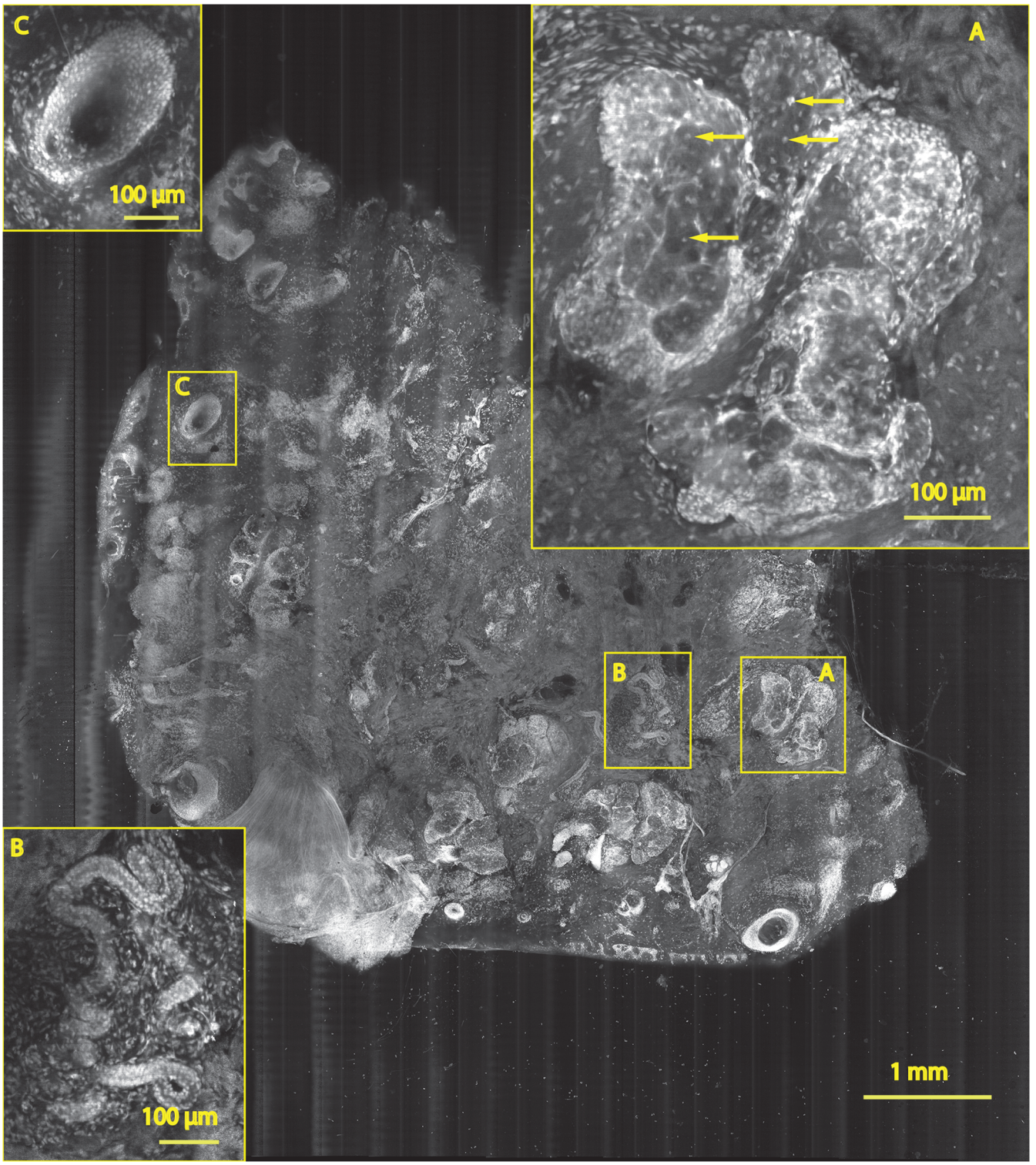

Fig. 7 A 6.8- × -8 mm^2 mosaic consisting of 17 fluorescence image strips of excised tissue from Mohs surgery. Typical features such as sebaceous glands (a), eccrine glands (b), and hair follicle (c) are seen. The mosaic dimensions are 7300- × -8200 pixels (width × height) with 8 bits/pixel. The features in the mosaic compare well to the pathology (Fig. 8), in terms of location, shape, size, nuclei of cells (shown with arrows), and overall morphology.

the center region of each strip. This also serves the purpose of restricting the possible offset solutions to those that we know are most likely to be a good match. The search region is further restricted to coordinates near that expected from our knowledge of the stage motion. Generally, an apodizing window function is applied to an image before performing a phase-correlation algorithm to reduce high-frequency edge effects. However, in this case, the illumination fall-off across the strips serves this purpose.

The illumination fall-off is corrected after the registration algorithm is applied. Because the optical scanning through the objective lens is in one dimension only, the illumination fall-off is along only the x direction of each strip. The fall-off is corrected by averaging each strip along its length, normalizing, and dividing each line in the strip by the normalized average fall-off profile of the strip.

In the overlap region between strips, the strips are blended by a weighted average of the overlapping pixels determined by the pixel distance to the edge of the strip. Pixels close to the edge of the strip are weighted less than pixels farther away. The result is a seamless mosaic, with more weight given to pixels near the center of the strip and less weight given to pixels near the edges of the strip.

2.5 *Display of Mosaics*

The mosaics are displayed in 8-bits on a large monitor with 2500×1600 pixels (30-in. flat-screen Dell 222–7175, with a GeForce 8800 GTS video card).When histopathology is examined with a bright field microscope, using, typically, a 2×, 0.08NA objective lens with white light illumination, the observed field of view (FOV) is 10 mm with ~4-μm resolution. This FOV consists of approximately 2500×2500 pixels assuming one pixel per one optical resolution point. Our display matches this standard 2×-view of histopathology. Zooming allows one to view submosaics at full resolution, mimicking the pathologist's ability to switch to higher magnifications when necessary. Our Matlab program can easily manage the manipulation and display of mosaics of FOV 10×10 mm. However, for larger mosaics, the program exhausts allowed allocated memory in our current system. (Potential future implementation at the bedside in, say, diverse and low-resource

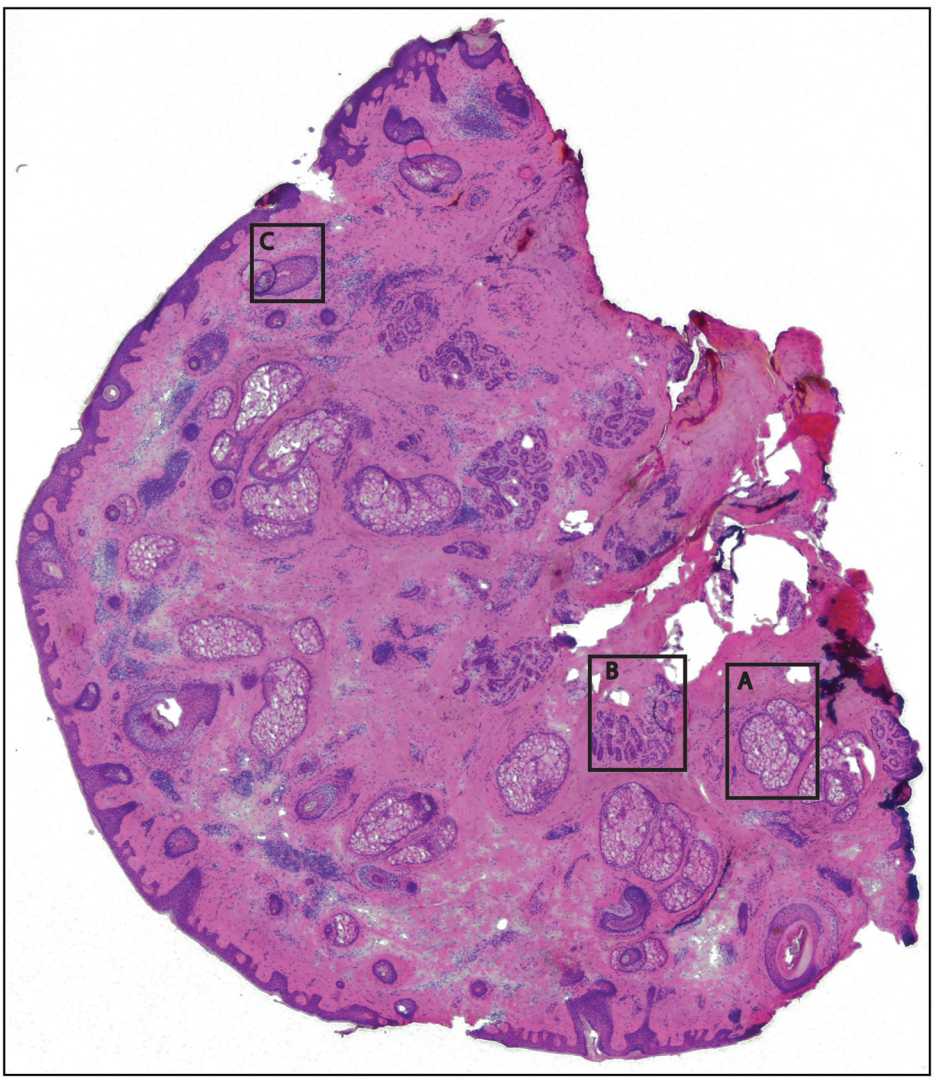

Fig. 8 Frozen H&E-stained pathology of excised tissue from Mohs surgery. The frozen section corresponds to a tissue slice adjacent to (but not exactly of the) imaged surface shown in Fig. 7. The features in inset areas A, B, and C are clearly identified across the two figures.

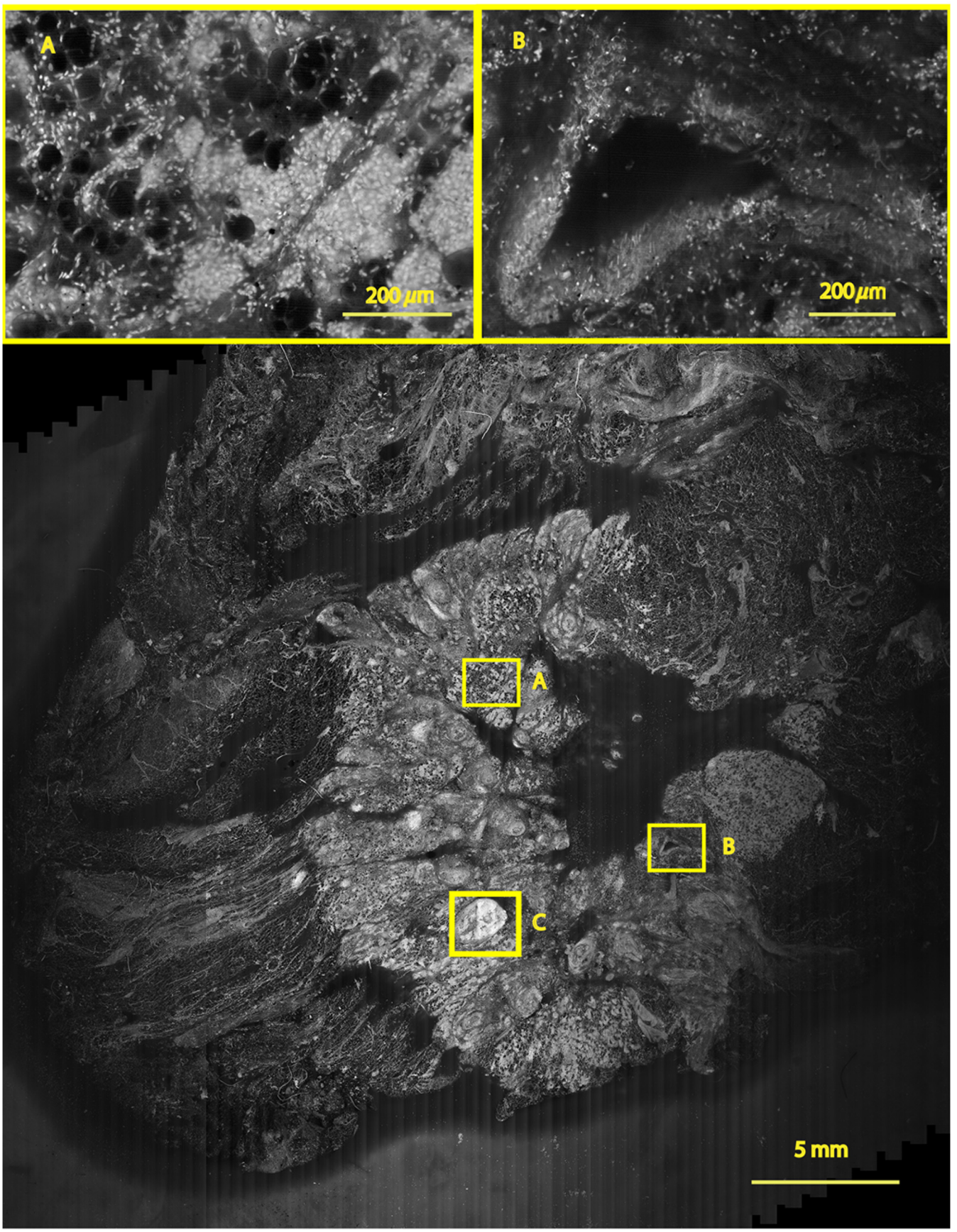

Fig. 9 A 2.5 × 3.5 cm^2 mosaic, consisting of 85 fluorescence image strips, of excised tissue from breast cancer surgery. The mosaic shows a central bright-appearing region of tumor and outlying somewhat darker-appearing regions of fat and fibrous tissue. The nucleus of cells appear to be bright. Closer inspection (insets) shows: (a) cancer cells invading a region of fat cells (b) a breast duct with hollow lumen (c) cancer cells proliferating in a duct. (*Continued on next page*.)

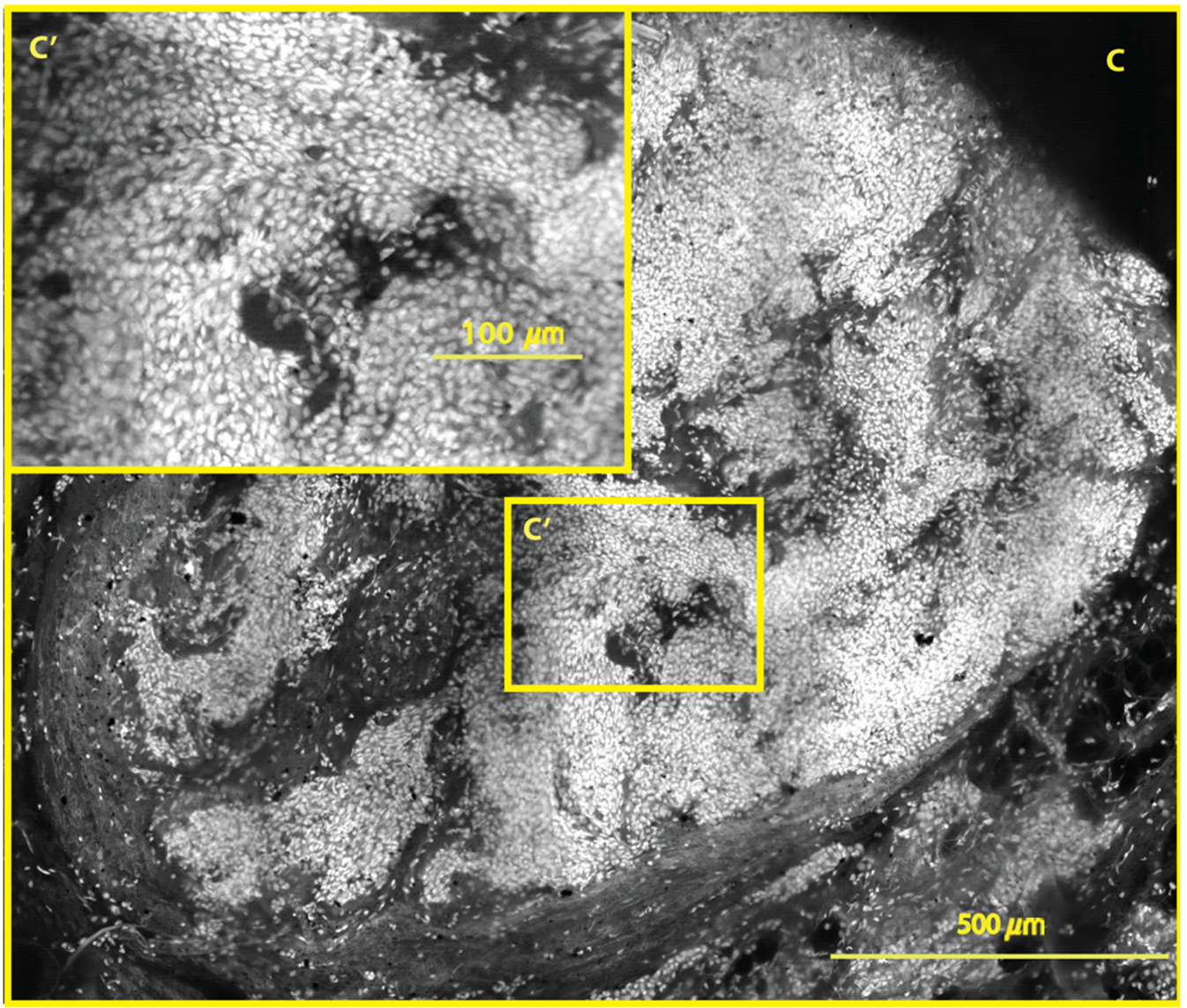

Fig. 9 (*Continued.*)

settings may require alternative practical and lower-cost approaches. One approach, for example, is scaling large mosaics to smaller size, while maintaining pathology-equivalent 2500×2500 pixelation, which results in final size of 3 to 4 MB. This approach has been validated for adequate clinical quality and sensitivity and specificity by our Mohs surgeons.[18,19]

3 Results

Figures 5 to 10 show examples of strip mosaics of varying sizes, with their corresponding hematoxylin and eosin (H&E)-stained pathology. The mosaics are shown in fluorescence contrast, following staining with acridine orange. The resolution and nuclear-level morphology in the mosaics may not be easily appreciated in these figures, but is more clearly seen when viewed on our large monitor with adequate pixelation. In these figures, we include inset areas that are displayed with zoom to show the resolution and level of detail.

3.1 *Skin Tissue from Mohs Surgery*

Figure 5 shows a strip mosaic of a skin excision from Mohs surgery. The measured time for the 7.7×7.7 mm^2 mosaic, consisting of 24-strip images, was about 3 min. This mosaic was created before we implemented simultaneous stitching with the acquisition. The strips were stitched after acquisition was completed, adding approximately an extra 96 s to complete the mosaic.

Nuclear detail and morphology is seen in the magnified insets A, B, and C. The morphologic features in the mosaics compare well to those in the corresponding pathology (Fig. 6) for both basal cell carcinomas and normal skin. However, a perfect one-to-one correlation of individual features is not always expected (nor desired by Mohs surgeons), because tissue is pliant and thus susceptible to distortions introduced during the fixturing for mosaicing or processing for frozen sections. As a result, the pathology is usually of a 5-μm-thin tissue section that may be adjacent to, but not exactly of, the imaged surface.

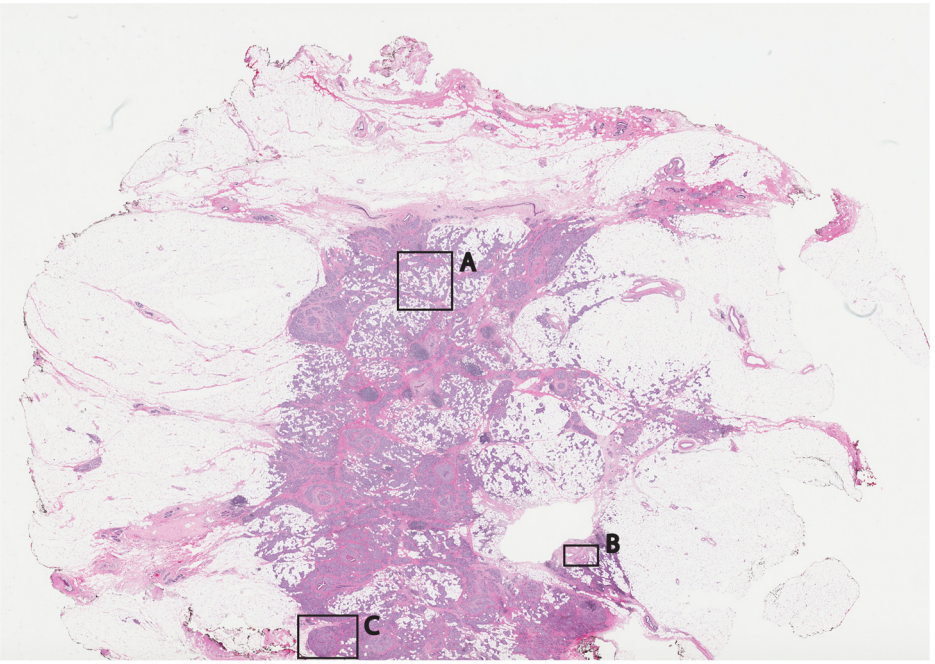

Fig. 10 Fixed H&E-stained pathology of excised tissue from breast surgery. Labels indicate matching regions to the confocal mosaic in Fig. 9: (a) a duct; (b) ductal carcinoma *in situ*; and (c) invasive cancer cells.

Figure 7 is also a strip mosaic of a skin excision from Mohs surgery. This mosaic is 6.8- × -8 mm^2 consisting of 17-strip images. The image strips were stitched simultaneously with acquisition, and the mosaic was completed in 55 s [The simultaneous stitching eliminating the extra time that was otherwise required for some of our earlier mosaics (Fig. 8)]. The nuclear detail and morphology is seen in the magnified insets A, B, and C. The morphologic features in the mosaics compare well to corresponding pathology (Fig. 8).

3.2 *Breast Tissue from Breast Cancer Surgery*

Figure 9 is a strip mosaic of breast tissue from a lumpectomy. The actual size of the tissue is about 2.5×3.5 cm^2. A step-shaped artifact can be seen at the upper and lower edges of the mosaic (Fig. 9). This was due to a malfunction in the tissue translation stage. [The malfunction manifested as a loss of position in the scan along the strip (y direction) while stepping in the orthogonal direction (x direction.)] Thirty 3.5-cm-long image strips were acquired in 13 min and stitched after acquisition. For this mosaic, we can only report the acquisition time due to hardware limitation in the present implementation. The scan of a such large area requires about 60 image strips. Our stitching program (written in Matlab) runs out of allowed allocated memory during attempts to stitch all the 2.5-cm long strips. Each strip is a factor of 2.5 longer than our usual 10-mm strip. In this mosaic we first stitched four 2.5-cm strips and used ImageJ to merge 4-strip images together to create the mosaic. In the future, this hurdle may be overcome by implementing a graphic processing unit (GPU) dedicated for stitching and display. Since the strips are being stitched during acquisition we expect the full 2.5×3.5 cm^2 mosaic could be produced in 13 min with a dedicated GPU (plus the time to scan and stitch the last strip).

Within the mosaic, regions of interest can be identified. The central bright-appearing region is tumor and the outlying darker-appearing regions are primarily fat and connective tissue. Upon closer inspection, cellular and increased nuclear density is visible. For example, inset B of Fig. 9 shows a duct. A normal duct is made up of a double layer of cells surrounding an empty lumen. In this case, the normal growth of the epithelial cells has been disrupted and while the overall shape resembles a duct, the cellular architecture shows that this is no longer a typical cellular pattern. Inset C of Fig. 9 shows proliferation of cell growth in a duct. Instead of the normal double-cell layer, cells have grown inward to the lumen. The cells are contained within the boundaries of the duct, suggesting a ductal carcinoma *in situ*. Inset A of Fig. 9 shows invasive carcinoma in which the cancer cells have invaded the surrounding fat cells. The fat cells are large and appear dark. The tumor cells are small with bright nuclei.

4 Summary and Discussion

Our previous approaches for confocal mosaicing microscopy proved the feasibility of imaging nuclear and cellular morphology and tumor margins in large areas of freshly excised tissue.[13–15,21,22] Two Mohs surgeons demonstrated their ability to read mosaics in a manner similar to their examination of pathology, and detect basal cell carcinoma margins in Mohs surgical excisions with high sensitivity and specificity.[18,19] Although mosaicing could be performed in several minutes, the speed was still too slow to enable routine and practical use in Mohs and other surgical settings. To overcome this barrier and address the request for shorter times of surgeons, we designed a faster approach called "strip mosaicing." The initial feasibility was reported last year.[20] In this paper, we presented further advances in electronics, mechanics, custom software, and the overall integration of hardware and software into an approach that offers further improvement in speed.

Strip mosaicing confocal microscopy offers an imaging technology platform for rapid detection of tumor margins directly in fresh tissue during surgery. Large amounts of tissue may be

examined quickly enough to be of practical use in diverse surgical settings. The imaging may potentially be developed into an adjunct for pathology, to enable more complete and accurate removal of tumor. Further improvements in strip mosaicing may be achieved in several ways:

1. Increasing the speed of the polygon scanner (which is currently the limiting factor).
2. Employing other faster scanning methods.
3. Increasing the field-of-view while accepting lower but clinically acceptable resolution.
4. Automating the process for tissue mounting, flattening and leveling the imaging surface.

As shown in this paper, tissues from Mohs surgery and breast tumors are good tests to demonstrate strip mosaicing indifferent surgical settings. This approach may also find applications in other tissues, and not only in surgical settings but also in clinics for rapid screening of biopsies. Each application will, of course, present its own challenges in terms of the mechanical properties (shape, size, topography, compliance) of the tissue to be imaged, availability and efficacy of contrast agents, speed requirement and tissue fixturing for translation to the bedside. Currently there are many mosaicing approaches being developed for microscopy of processed tissue[23–33] as well as for *in vivo*.[34–39] Our instrumentation design will help in developing those approaches.

Beyond imaging excised tissue, a similar approach may be possible on patients to delineate tumor margins *in vivo*, either preoperatively or intraoperatively in surgical wounds. Preliminary feasibility of such techniques has been reported for mosaicing on skin *in vivo*[17,34–39] and also in shave-biopsied wounds in which residual tumor (basal and squamous cell carcinoma) margins were delineated.[40] In the future, an approach that involves mosaicing both on excised tissue at the bedside and intra-operatively on the patient may prove useful for detecting tumor margins in a rapid, efficient, and cost-effective manner.

Acknowledgments

The authors gratefully acknowledge support from NIH grant R01EB012466 from NIBIB's Image Guided Interventions Program (Program Director Dr. Steve Krosnick). We thank Drs. Kishwer Nehal and Erica Lee for supplying discarded tissue from Mohs surgery, and Drs. Melissa Murray and Monica Morrow for supplying tissue from breast cancer surgeries (under IRB-approved protocols), and, most importantly, for their enthusiastic collaborative involvement with image analysis and correlation to pathology. We are grateful to Dr. Chris Glazowski for help with assembly and alignment of the microscope, Bill Fox and Scott Grodevant at Lucid Inc. and our machine shop at MSKCC for technical support.

References

1. M. Rajadhyaksha et al., "Confocal examination of nonmelanoma cancers in thick skin excisions to potentially guide mohs micrographic surgery without frozen histopathology," *J. Investig. Dermatol.* **117**(5), 1137–1143 (2001).
2. R. Haque et al., "Surgical margins and survival after head and neck cancer surgery," *BMC Ear Nose Throat Disord.* **6**, 2 (2006).
3. L. Jacobs, "Positive margins: the challenge continues for breast surgeons," *Ann. Surg. Oncol.* **15**(5), 1271–1272 (2008).
4. M. Y. Al-Arashi, E. Salomatina, and A. N. Yaroslavsky, "Multimodal confocal microscopy for diagnosing nonmelanoma skin cancers," *Laser. Surg. Med.* **39**(9), 696–705 (2007).
5. M. Jain et al., "Multiphoton microscopy in the evaluation of human bladder biopsies," *Arch. Pathol. Lab. Med.* **136**(5), 517–526 (2012).
6. M. Jain et al., "Modified full-field optical coherence tomography: a novel tool for rapid histology of tissues," *J. Pathol. Inform.* **2**, 28 (2011).
7. D. Kang et al., "Comprehensive imaging of gastroesophageal biopsy samples by spectrally encoded confocal microscopy," *Gastrointest. Endosc.* **71**(1), 35–43 (2010).
8. T. Makino et al., "Multiphoton tomographic imaging: a potential optical biopsy tool for detecting gastrointestinal inflammation and neoplasia," *Cancer Prev. Res. (Phila.)* **5**(11), 1280–1290 (2012).
9. R. Patalay et al., "Multiphoton multispectral fluorescence lifetime tomography for the evaluation of basal cell carcinomas," *PloS one* **7**(9), e43460 (2012).
10. M. A. Saldua et al., "Imaging inflammation in mouse colon using a rapid stage-scanning confocal fluorescence microscope," *J. Biomed. Opt.* **17**(1), 016006 (2012).
11. M. T. Tilli et al., "Real-time imaging and characterization of human breast tissue by reflectance confocal microscopy," *J. Biomed. Opt.* **12**(5), 051901 (2007).
12. H. Yoo et al., "Reflectance confocal microscopy for the diagnosis of eosinophilic esophagitis: a pilot study conducted on biopsy specimens," *Gastrointest. Endosc.* **74**(5), 992–1000 (2011).
13. Y. G. Patel et al., "Confocal reflectance mosaicing of basal cell carcinomas in Mohs surgical skin excisions," *J. Biomed. Opt.* **12**(3), 034027 (2007).
14. D. S. Gareau et al., "Confocal mosaicing microscopy in Mohs skin excisions: feasibility of rapid surgical pathology," *J. Biomed. Opt.* **13**(5), 054001 (2008).
15. D. S. Gareau et al., "Confocal mosaicing microscopy in skin excisions: a demonstration of rapid surgical pathology," *J. Microsc.* **233**(1), 149–159 (2009).
16. A. N. Yaroslavsky et al., "Combining multispectral polarized light imaging and confocal microscopy for localization of nonmelanoma skin cancer," *J. Biomed. Opt.* **10**(1), 014011 (2005).
17. K. E. Loewke et al., "Real-time image mosaicing for medical applications," *Stud. Health Technol. Inform.* **125**, 304–309 (2007).
18. J. K. Karen et al., "Detection of basal cell carcinomas in Mohs excisions with fluorescence confocal mosaicing microscopy," *Br. J. Dermatol.* **160**(6), 1242–1250 (2009).
19. D. S. Gareau et al., "Sensitivity and specificity for detecting basal cell carcinomas in Mohs excisions with confocal fluorescence mosaicing microscopy," *J. Biomed. Opt.* **14**(3), 034012 (2009).
20. S. Abeytunge et al., "Rapid confocal imaging of large areas of excised tissue with strip mosaicing," *J. Biomed. Opt.* **16**(5), 050504 (2011).
21. J. Bini et al., "Confocal mosaicing microscopy of human skin ex vivo: spectral analysis for digital staining to simulate histology-like appearance," *J. Biomed. Opt.* **16**(7), 076008 (2011).
22. D. S. Gareau, "Feasibility of digitally stained multimodal confocal mosaics to simulate histopathology," *J. Biomed. Opt.* **14**(3), 034050 (2009).
23. G. Babaloukas et al., "Evaluation of three methods for retrospective correction of vignetting on medical microscopy images utilizing two open source software tools," *J. Microsc.* **244**(3), 320–324 (2011).
24. A. Bennassar et al., "Rapid diagnosis of two facial papules using ex vivo fluorescence confocal microscopy: toward a rapid bedside pathology," *Dermatol. Surg.* **38**(9), 1548–1551 (2012).
25. M. L. Berlanga et al., "Three-dimensional reconstruction of serial mouse brain sections: solution for flattening high-resolution large-scale mosaics," *Front. Neuroanat.* **5**(17), 1–8 (2011).
26. S. K. Chow et al., "Automated microscopy system for mosaic acquisition and processing," *J. Microsc.* **222**(Pt 2), 76–84 (2006).
27. S. Debarbieux et al., "Perioperative confocal microscopy of the nail matrix in the management of in situ or minimally invasive subungual melanomas," *Br. J. Dermatol.* **167**(4), 828–836 (2012).
28. W. Y. Hsu, W. F. P. Poon, and Y. N. Sun, "Automatic seamless mosaicing of microscopic images: enhancing appearance with colour degradation compensation and wavelet-based blending," *J. Microsc.* **231**(3), 408–418 (2008).

29. P. Khurdet et al., "Global error minimization in image mosaicing using graph connectivity and its applications in microscopy," *J. Pathol. Inform.* **2**, S8 (2011).
30. F. Piccinini et al., "Multi-image based method to correct vignetting effect in light microscopy images," *J. Microsc.* **248**(1), 6–22 (2012).
31. J. L. Schroederet al., "Rapid overlapping-volume acquisition and reconstruction (ROVAR): automated 3-D tiling for high-resolution, large field-of-view optical microscopy," *J. Microsc.* **243**(1), 103–110 (2011).
32. H.-C. Shao, W.-L. Hwang, and Y.-C. Chen, "Optimal multiresolution blending of confocal microscope images," *IEEE Trans. Biomed. Eng.* **59**(2), 531–541 (2012).
33. C. Sun et al., "Mosaicing of microscope images with global geometric and radiometric corrections," *J. Microsc.* **224**(2), 158–165 (2006).
34. V. Becker et al., "High-resolution miniprobe-based confocal microscopy in combination with video mosaicing (with video)," *Gastrointest. Endosc.* **66**(5), 1001–1007 (2007).
35. N. Bedard et al., "Real-time video mosaicing with a high-resolution microendoscope," *Biomed. Opt. Express* **3**(10), 2428–2435 (2012).
36. P. Kim et al., "In vivo wide-area cellular imaging by side-view endomicroscopy," *Nat. Meth.* **7**(4), 303–305 (2010).
37. K. E. Loewke et al., "In vivo micro-image mosaicing," *IEEE Trans. Biomed. Eng.* **58**(1), 159–171 (2011).
38. T. Vercauteren et al., "Robust mosaicing with correction of motion distortions and tissue deformations for in vivo fibered microscopy," *Med. Image Anal.* **10**(5), 673–692 (2006).
39. T. Vercauteren et al., "Mosaicing of confocal microscopic in vivo soft tissue video sequences," in *Medical Image Computing and Computer-Assisted Intervention—Miccai 2005, Pt 1*, J. S. Duncan and G. Gerig, Eds., pp. 753–760, Springer-Verlag, Berlin, Germany (2005).
40. A. Scope et al., "In vivo reflectance confocal microscopy of shave biopsy wounds: feasibility of intraoperative mapping of cancer margins," *Br. J. Dermatol.* **163**(6), 1218–1228 (2010).